Volume 6
Number 6
June 2025
Pages 825–998

RSC Chemical Biology

rsc.li/rsc-chembio

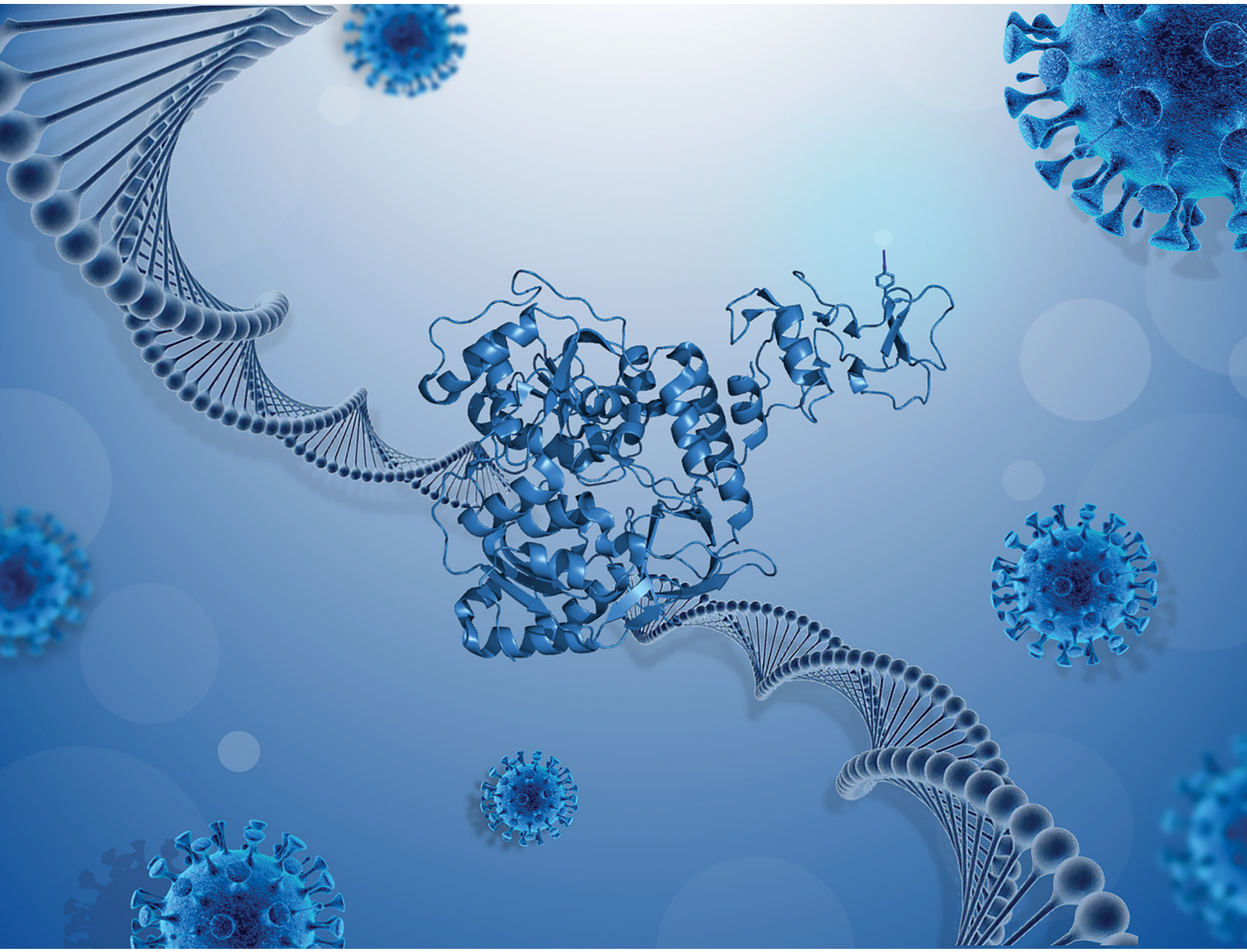

ISSN 2633-0679

ROYAL SOCIETY OF CHEMISTRY

PAPER
John Paul Pezacki *et al.*
Monitoring SARS-CoV-2 Nsp13 helicase binding activity using expanded genetic code techniques

RSC Chemical Biology

ROYAL SOCIETY OF CHEMISTRY

PAPER

View Article Online
View Journal | View Issue

Cite this: *RSC Chem. Biol.*, 2025, **6**, 860

Monitoring SARS-CoV-2 Nsp13 helicase binding activity using expanded genetic code techniques†

Eryn Lundrigan, Christine Hum, Nadine Ahmed and John Paul Pezacki *

The severe acute respiratory syndrome coronavirus 2 (SARS-CoV-2) non-structural protein 13 (Nsp13) helicase is a multi-functional protein that can unwind dsDNA and dsRNA in an NTP-dependent manner. Given that this viral helicase is essential for viral replication and highly conserved among coronaviruses, a thorough understanding of the helicase's unwinding and binding activity may allow for the development of more effective pan-coronavirus therapeutics. Herein, we describe the use of genetic code expansion techniques to site-specifically incorporate the non-canonical amino acid (ncAA) *p*-azido-L-phenylalanine (AzF) into Nsp13 for fluorescent labelling of the enzyme with a conjugated Cy5 fluorophore. This Cy5-labelled Nsp13-AzF can then be used in Förster resonance energy transfer (FRET) experiments to investigate the dynamics of enzyme translocation on its substrate during binding and unwinding. Five sites (F81, F90, Y205, Y246, and Y253) were identified for AzF incorporation in Nsp13 and assessed for fluorescent labelling efficiency. The incorporation of AzF was confirmed to not interfere with the unwinding activity of the helicase. Subsequently, FRET-based binding assays were conducted to monitor the binding of Cy5-labelled Nsp13-AzF constructs to a series of fluorescently-labelled nucleic acid substrates in a distance-dependent manner. Overall, this approach not only allows for the direct monitoring of Nsp13's binding activity on its substrate, it may also introduce a novel method to screen for compounds that can inhibit this essential enzymatic activity during viral replication.

Received 11th January 2025,
Accepted 18th April 2025

DOI: 10.1039/d4cb00230j

rsc.li/rsc-chembio

Introduction

Severe acute respiratory syndrome coronavirus 2 (SARS-CoV-2) is the etiological agent responsible for the coronavirus disease of 2019 (COVID-19) pandemic, which has caused extensive economic and health-related hardships worldwide.[1–3] Originating in late 2019, this virus has infected over 704 million people and caused over 7 million deaths.[4,5] Despite the development of vaccines and therapeutics against SARS-CoV-2, this virus remains a significant threat to human health as novel variants continue to emerge and evade developed therapeutics. As a result, there is a need to better understand this virus' mechanism of pathogenesis to develop more effective pan-coronavirus therapeutics. RNA viruses, such as SARS-CoV-2, often encode their own RNA helicase as they play important roles in viral replication.[6,7] The SARS-CoV-2 Nsp13 helicase is a multi-functional protein that possesses an N-terminal zinc-binding domain (ZBD) and C-terminal nucleoside triphosphatase (NTPase) domains.[8–10] This helicase hydrolyzes nucleoside triphosphates (NTPs) to unwind double-stranded (ds) nucleic acids (both DNA and RNA) in the 5′ to 3′ direction to allow for the replication of the viral genome.[11–14] Additionally, Nsp13 plays a pivotal role in the 5′-capping of viral messenger RNA (mRNA), through its RNA 5′-triphosphatase activity,[10,15–18] and can associate with the viral replication-transcription complex (RTC) to facilitate genomic replication and RNA-dependent RNA polymerase (RdRp) backtracking to allow for template switching and proofreading of the viral genome.[19,20] As Nsp13 is highly conserved among coronaviruses,[10,21] it is often thought to be an ideal therapeutic target.[22,23] However, despite this therapeutic potential, its specific mechanism of binding and unwinding has yet to be fully characterized.

Several approaches have been employed to investigate the catalytic mechanism by which the Nsp13 helicase unwinds nucleic acids. Recent cryo-electron microscopy studies uncovered that Nsp13 directly interacts with the RTC to facilitate the unwinding of the viral genome, potentially through mechanoregulation by the RdRp.[11,20,24,25] From high-resolution X-ray crystal structures and hydrogen–deuterium (H/D) exchange assays, an inchworm-type model for Nsp13 translocation along ssRNA in the 5′ to 3′ direction was suggested.[25,26] Collectively, these studies provide enormous insight into Nsp13's enzymatic activities; however, they are limited to reporting the average activities of a heterogenous population and cannot distinguish the activity of a single Nsp13 molecule. This poses a great limitation for multi-domain and multi-functional enzymes, such as Nsp13, which

Department of Chemistry and Biomolecular Sciences, University of Ottawa, Ottawa, Ontario K1N 6N5, Canada. E-mail: john.pezacki@uottawa.ca

† Electronic supplementary information (ESI) available. See DOI: https://doi.org/10.1039/d4cb00230j

cycles through different catalytic states during nucleotide binding and unwinding,[10,11] highlighting the need for single-molecule experiments to monitor the dynamics of individual enzyme–substrate complexes.

Previous single molecule techniques, such as optical tweezer and single-molecule Förster resonance energy transfer (smFRET), have provided valuable data on Nsp13 unwinding activity. Additionally, recent work using nanopore-based approaches has revealed single-nucleotide steps of Nsp13 unwinding and translocation along DNA (Marx *et al.*, 2023).[27] These studies have significantly advanced our understanding of Nsp13 function, yet each technique has inherent limitations. Optical tweezers apply external force, which may alter the enzymes natural conformational dynamics, while nanopore-based methods require a specific experimental setup that may not capture all intermediate states of helicase function. The dynamic nature of Nsp13's transitions between different catalytic states during nucleotide binding and unwinding underscore the need for complementary single-molecule techniques that provide additional mechanistic insights.

While previous studies have provided foundational insights, a critical knowledge gap remains in directly monitoring the transient interactions and real-time positioning of Nsp13 on its nucleic acid substrates. This gap is significant because achieving such goal would offer a more comprehensive understanding of the helicase's activity and regulatory mechanisms. The present study aims to address this gap by developing a fluorescence-based FRET assay, an approach that has been successfully used for the characterization of other enzymes,[26,28,29] to observe the binding dynamics of fluorescently labeled Nsp13 with its nucleic acid substrates. We establish site-specific labeling using genetic code expansion, in order to achieve FRET. The FRET assay for NSP13 reported herein paves the way for future extensive and detailed studies including screening for inhibitors as well as single molecule experiments that will allow for the tracking of transient molecular movements along catalytic pathways.

In this study, we utilize genetic code expansion techniques to site-specifically incorporated the non-canonical amino acid (ncAA) *p*-azido-L-phenylalanine (AzF) into Nsp13 to act as a bioorthogonal handle for fluorescent labelling.[30,31] Next, we assessed the labelling efficiency of the Nsp13-AzF constructs with a Cy5-dibenzocyclooctyne (DBCO) conjugated dye and confirmed that helicase unwinding activity was not altered with the incorporation of AzF. After identifying suitable Nsp13-AzF constructs, FRET assays were used to characterize Nsp13 binding interactions with nucleic acid substrates in a distance-dependent manner.

Identifying and screening potential sites for the incorporation of AzF into Nsp13

First, we identified potential sites for AzF incorporation in Nsp13 that would be suitable to serve as a reactive site-specific bioorthogonal handle for fluorescent labelling. Using published crystal structures of the SARS-CoV-2 Nsp13 helicase,[11,20,32] we identified all the Tyr (Y) and Phe (F) residues in the structure as these two residues most closely resemble the structure of AzF, consequently minimizing any structural or functional changes to the enzyme. To further narrow down potential candidates, we selected residues that were within FRET distance (10–100 Å) to the modelled RNA in the structure, were solvent or surface accessible for subsequent click chemistry reactions and were primarily located in the flexible loop regions of the protein. Furthermore, catalytic residues, such as those involved in ATP hydrolysis and nucleotide binding, were avoided to prevent altering the enzymatic activities of this helicase. In the end, residues F81, F90, Y205, Y246, and Y253 were selected as sites for AzF incorporation (Fig. 1A). To determine if AzF was successfully incorporated into Nsp13, full-length wild type (WT) and Nsp13-AzF protein expression was assessed in bacterial cell lysates in the presence and absence of AzF in the growth media,

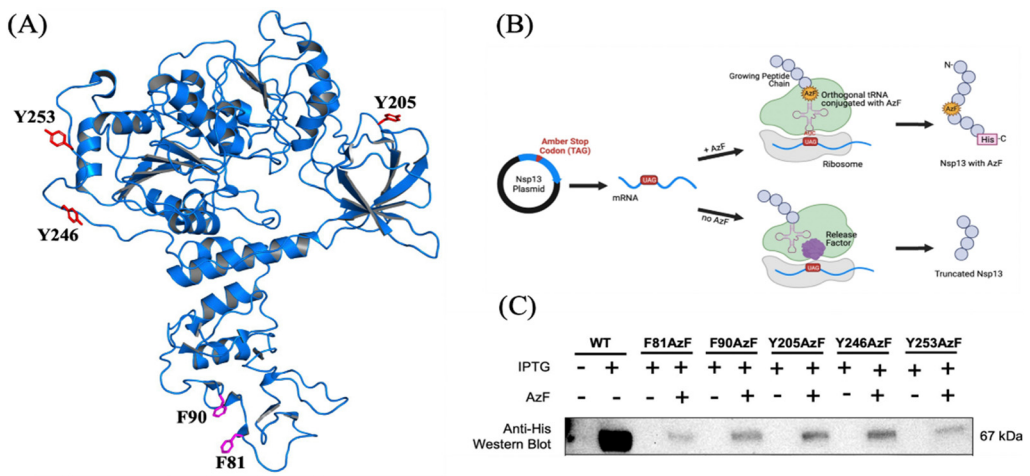

Fig. 1 Site-specific incorporation of AzF into Nsp13. (A) Five sites were identified for AzF incorporation in SARS-CoV-2 Nsp13 (PDB: 6XEZ). Phe (F, purple) and Tyr (Y, red) residues that are within FRET distance to modelled RNA in the crystal structure, are surface accessible, and were primarily located in the flexible loop regions of the protein were selected for AzF incorporation. (B) Schematic depicting the incorporation of AzF into C-terminal His-tag Nsp13. (C) Western blot showing full-length protein expression of Nsp13-AzF constructs in bacterial lysates in the presence and absence of AzF in the growth media.

the protein sequence was prematurely terminated at the mutated TAG site, as it is a canonical stop codon, and therefore no protein was detected by western blot probing against the C-terminal His-tag of the Nsp13 helicase. However, when AzF was supplemented to the growth media, AzF was incorporated at the mutated TAG site allowing for full-length protein expression (Fig. 1B). Full-length expression of all five Nsp13-AzF constructs was observed. No canonical amino acids were incorporated into our specified sites of interest in the absence of added AzF as no protein expression was observed (Fig. 1C and Fig. S1, ESI†).

Screening Nsp13-AzF constructs for site-specific fluorescent labelling with Cy5-DBCO

WT Nsp13 and Nsp13-AzF constructs were purified from bacterial cell lysates and labelled with a Cy5-DBCO conjugated dye through strain-promoted alkyne-azide cycloaddition (SPAAC) (Fig. 2A). The labelling efficiencies of these Nsp13-AzF constructs were analyzed by western blot. Despite unequal Nsp13 protein abundance between samples, we observed minimal background Cy5 labelling of WT Nsp13 (Fig. 2B and Fig. S2, ESI†). Normalizing the Cy5 fluorescence signal to the total protein abundance demonstrated that all Nsp13-AzF constructs yielded higher labelling efficiencies compared to WT ranging from 7-fold greater with Y205AzF; 15- to 16-fold greater with F90AzF, Y246AzF and Y253AzF; and 18-fold greater with F81AzF (Fig. 2C).

The unwinding activity of F81AzF and Y253AzF were not affected by the incorporation of AzF

After confirming that Nsp13-AzF constructs could be efficiently labelled with Cy5-DBCO, we needed to ensure that the unwinding activity of these constructs was not affected by the incorporation of AzF. An unwinding assay was performed to monitor the rate each Nsp13-AzF construct unwinds a dsDNA substrate containing a black hole quencher and Cy3 fluorophore on opposite strands.[33] In this assay, as the dsDNA is unwound by Nsp13, the Cy3 strand is released generating a corresponding increase in Cy3 fluorescence (Fig. 3A). The unwinding activities of F81AzF, F90AzF, and Y253AzF were found to be the most similar to WT Nsp13, demonstrating unwinding rates of 0.42 ± 0.06 nM min^{-1}, 0.25 ± 0.03 nM min^{-1}, and 0.33 ± 0.05 nM min^{-1}, respectively, compared to the unwinding rate of 0.59 ± 0.14 nM min^{-1} observed with the WT (Fig. 3B). The two other Nsp13-AzF constructs, Y205AzF and Y246AzF, demonstrated a more gradual unwinding activity with rates of 0.04 ± 0.003 nM min^{-1} and 0.06 ± 0.005 nM min^{-1}, respectively (Fig. 3B). Altogether, F81AzF and Y253AzF were the two Nsp13-AzF constructs with the best labelling efficiency and unwinding rates most similar to WT Nsp13. Clicking on Cy5-DBCO to Nsp13 F81AzF does not change unwinding activity compared to Nsp13 F81AzF without Cy5 (Fig. S3–S5, ESI†).

Monitoring the binding of Nsp13-AzF to dsDNA substrates by FRET

After determining that Nsp13 F81AzF and Y253AzF both showed efficient Cy5-labelling and similar unwinding rates to WT Nsp13, a FRET-based assay was conducted with these constructs to monitor its binding to a series of Cy3-labelled substrates (Fig. 4A). This assay was done in the absence of ATP to observe Nsp13 substrate binding activity as opposed to helicase unwinding activity. A series of 20 nt long Cy3-labelled DNA substrates (S20-Cy3) with varying duplex lengths, denoted as "X*n*" where "*n*" refers to the length of the duplex region, were designed to assess the distance-dependent relationship of FRET efficiency (S20-Cy3/X5, S20-Cy3/X8, S20-Cy3/X10, S20-Cy3/X12, S20-Cy3/X15, S20-Cy3/X17, S20-Cy3/X20) (Fig. 4B). As the length of the duplex region increases, the ss-overhang region shortens, and the distance between the bound Cy5-labelled Nsp13 and the Cy3

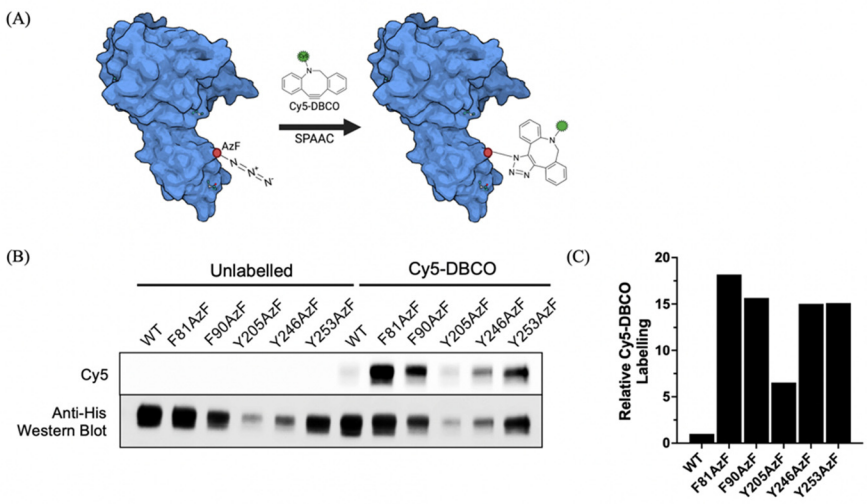

Fig. 2 Site-specific fluorescent labelling of Nsp13-AzF constructs with Cy5-DBCO. (A) Schematic depicting the fluorescent labelling of Nsp13-AzF constructs through SPAAC reactions with a Cy5-DBCO conjugated dye. (B) Purified WT Nsp13 and Nsp13-AzF constructs were incubated with Cy5-DBCO at a molar ratio of 1 : 2 protein to dye. A Cy5 fluorescence scan was used to assess the labelling efficiency of the constructs. (C) Densitometry analysis was performed by normalizing the Cy5 intensity to the total protein abundance. The adjusted intensity is presented relative to the WT control.

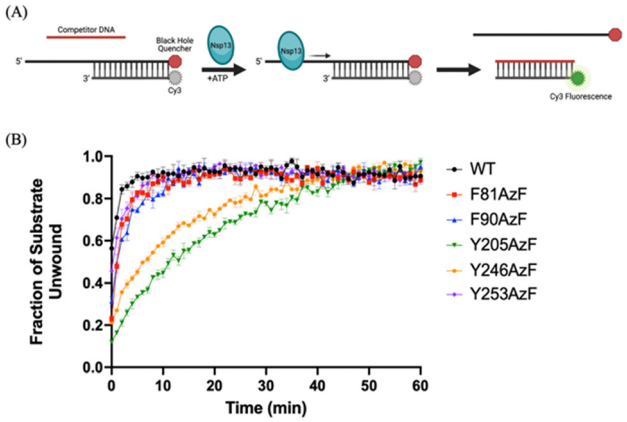

Fig. 3 F81AzF and Y253AzF demonstrate similar unwinding rates to WT Nsp13. (A) Schematic depicting the Nsp13 helicase unwinding assay. As Nsp13 unwinds a dsDNA substrate containing a black hole quencher and Cy3 fluorophore on opposite strands, the Cy3 strand is released generating a corresponding increase in Cy3 fluorescence. The competitor DNA captures the free Cy3 strand to prevent the substrate from re-annealing. (B) The unwinding activity of purified WT Nsp13 and Nsp13-AzF constructs was monitored. 5 nM of purified protein was incubated with 50 nM of dsDNA substrate and the reaction was initiated with the addition of 0.1 mM ATP. The graph is presented as the fraction of substrate unwound over time. Data is presented as mean ± SD (n = 3). Fluorescence values were fitted using a one-phase association on PRISM-GraphPad (v9.4.1) to determine unwinding rates.

dye on the 3′ terminus of the substrate would also increase thereby reducing FRET efficiency (Fig. 4A). First, we determined the ratiometric intensity-based FRET proximity ratio (E_{PR}), or FRET value, for the binding of Cy5-labelled WT Nsp13, F81AzF, and Y253AzF to a series of Cy3-labelled dsDNA substrates of varying duplex lengths. With WT Nsp13, an E_{PR} value of ∼0.08 was observed with the fully duplexed substrate (S20-Cy3/X20). The E_{PR} values for WT Nsp13 remained low and constant (∼0.12–0.13) as the substrate's duplex length increased (X5-X17) (Fig. 4B). The E_{PR} value of F81AzF and Y253AzF decreased in a distance-dependent manner as the length of the duplex region increased. For F81AzF, we determined a maximal E_{PR} value of ∼0.35 with the S20-Cy3/X5 substrate as compared to the residual E_{PR} of ∼0.14 with the fully duplexed substrate (S20-Cy3/X20) (Fig. 4B). For Y253AzF, we determined a maximal E_{PR} value of ∼0.28 with the S20-Cy3/X5 substrate as compared to the residual E_{PR} of ∼0.12 with the fully duplexed substrate (S20-Cy3/X20) (Fig. 4B). Next, we evaluated how the FRET signal changes with varying protein concentrations. For all substrates, the E_{PR} value increased in a protein concentration-dependent manner for both F81AzF and Y253AzF, with a consistently higher E_{PR} value observed with F81AzF (Fig. 4C). The corresponding fluorescence emission spectra corroborate these findings and show that the F81AzF construct generates a protein concentration-dependent decrease in the Cy3 signal at 565 nm with a corresponding increase in the Cy5 signal at 670 nm, which is indicative of FRET (Fig. 4D and Fig. S6, ESI†). Altogether, the F81AzF construct demonstrated the best distance-dependent FRET efficiency, making it a viable candidate for future smFRET experiments to monitor the direct binding and positioning of a Nsp13 molecule on its substrate.

Discussion

The incorporation of ncAAs, such as AzF, into proteins can provide numerous potential applications. One of these highly useful applications includes the ability to serve as a site-specific bioorthogonal reactive handle for fluorescent labelling.[34,35] This is especially useful for studying the transient dynamics of enzyme and nucleic acid interactions as the site-specific labelling of each molecule with corresponding FRET-pair fluorophores allows for the direct monitoring of the enzyme along its bound substrate.

Five potential sites for incorporating AzF into the SARS-CoV-2 Nsp13 helicase were investigated (F81, F90, Y205, Y246, and Y253). Two of the selected residues, F81 and F90, were located in the fairly flexible ZBD of SARS-CoV-2 and have been shown to be on the interface involved with interactions between Nsp13 and Nsp8a in the RTC.[20] Y205 is found in the 1B domain and has been recently hypothesized to engage with residue W178 to form a platen that aids in the conformation-specific recognition of Z-RNA, the left-handed conformer of normal dsDNA.[36] Y246 and Y253 are both found on an exterior flexible loop in the 1B domain, next to the RecA-like 1A domain but away from conserved helicase motifs I, II, and III that make contact to bound nucleotides.[10] Full-length protein expression of all five Nsp13-AzF constructs was observed, but not to the same level as WT Nsp13, which was to be expected since these evolved tRNAs conjugated with AzF may compete with release factors that facilitate the termination of protein synthesis at the amber stop codon, TAG.[31,37] Additionally, changes to the folding competency of these Nsp13-AzF constructs may account for some of the variability in protein abundance observed.

Next, the reactivity of Nsp13-AzF constructs for a strained alkyne-conjugated dye, Cy5-DBCO, was assessed. When purified Nsp13-AzF was reacted with two-molar excess Cy5-DBCO, without the removal of unincorporated dye, we observed some background labelling of the unmodified WT Nsp13. This background labelling may be attributed to the fact that strained-alkynes can sometimes cross-react with nucleophiles, such as free thiols, *via* a Michael addition.[38] Therefore, as there are 26 cysteine residues in Nsp13, these thiol side chains may react with the strained alkyne leading to some unspecific background labelling as the unreacted dye was not removed.[39] Further optimization of the labelling conditions (*e.g.*, time, concentration *etc.*) and subsequent removal of unreacted dye may help mitigate this concern. Despite this, it is evident that the Nsp13-AzF constructs can be efficiently and specifically labelled with Cy5-DBCO, with F81AzF showing the best labelling efficiency.

When evaluating the unwinding activity of the Nsp13-AzF constructs, we identified that F81AzF and Y253AzF were the only constructs to have unwinding rates within a two-fold difference compared to the WT. Interestingly, the Y246AzF showed a substantially lowered unwinding activity despite this mutation being located in the same region as Y253AzF. Both of

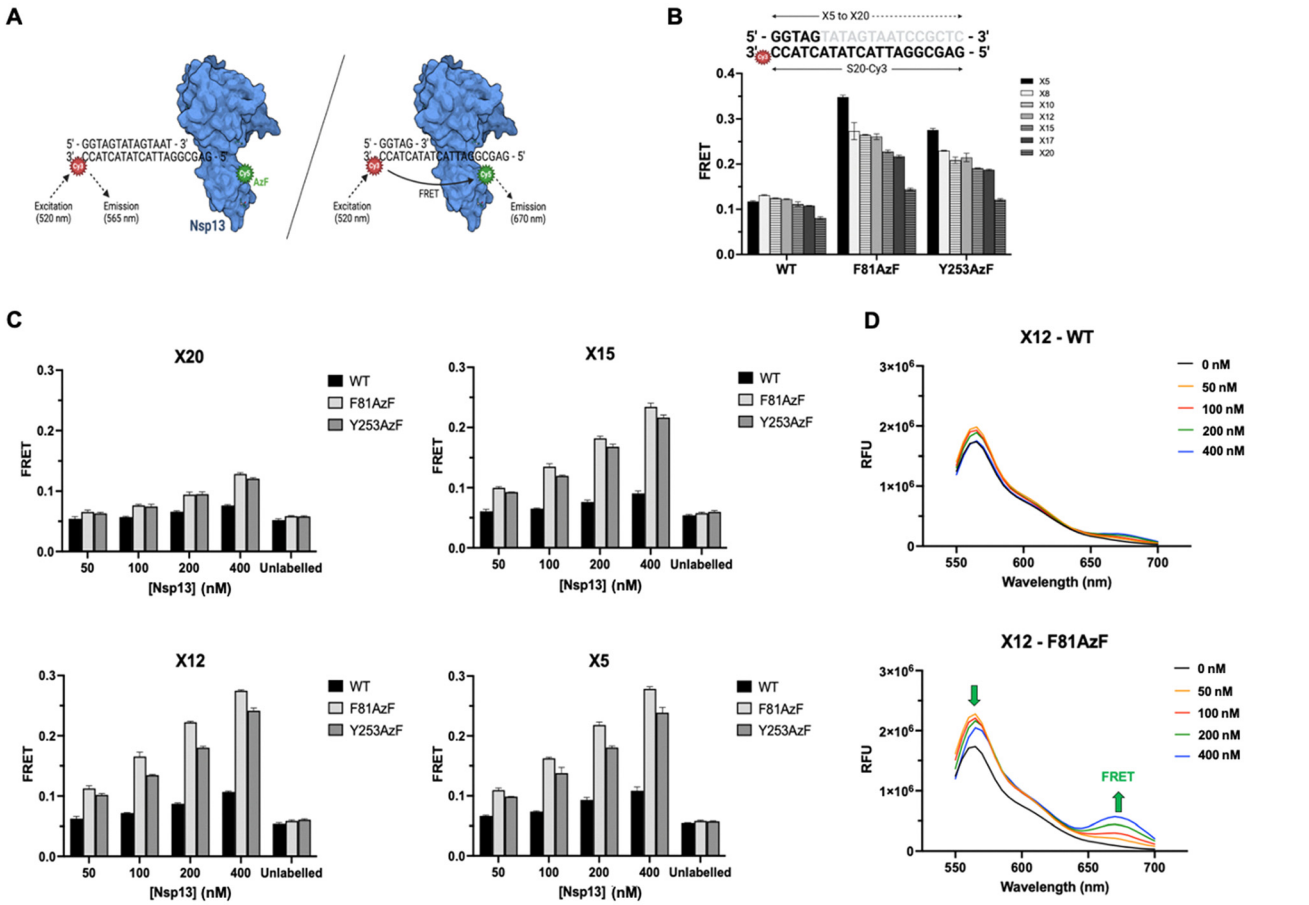

Fig. 4 Monitoring the binding of Cy5-labelled Nsp13 F81AzF and Y253AzF to Cy3-labelled dsDNA by FRET. (A) Schematic representation of the binding of Cy5-labelled Nsp13-AzF to dsDNA substrates. Upon excitation at 520 nm, if Nsp13 is bound to the ss-overhang of the substrate at a close enough distance to the Cy3 dye on the dsDNA substrate, FRET will be observed through emission of the Cy5 signal at 670 nm. (B) A series of DNA substrates with duplex lengths varying from 5 to 20 nt were used in FRET-based binding assays. The ratiometric intensity-based FRET proximity ratio (E_{PR}) was calculated to assess the binding of Cy5-labelled WT Nsp13, F81AzF, and Y253AzF to a series of dsDNA substrates. (C) The E_{PR} for the binding of Cy5-labelled WT Nsp13, F81AzF, and Y253AzF to dsDNA substrates with varying duplex lengths shows an increase in FRET with increasing protein concentration. Data are presented as mean ± SD (n = 3). (D) The emission spectra for the binding of Cy-5 labelled WT Nsp13 and F81AzF to the S20-Cy3/X12 substrate shows a Cy3 peak at 565 nm and a Cy5 peak at 670 nm.

these residues are not currently known to be directly involved in the unwinding process;[10,25,40] however, it may be interesting to further evaluate the kinetic implications of this Y246 residue on helicase activity in the future and see if the addition of AzF at this site changes the overall fold of the protein. Y205AzF demonstrated the lowest unwinding rate, which may correspond to its hypothesized role in binding dsRNA.[36] Altogether, we showed that unwinding activity is not compromised with the incorporation of AzF at sites F81 and Y253.

After screening for suitable Nsp13-AzF constructs, F81AzF and Y253AzF were selected for use in FRET-based binding assays. When comparing the E_{PR} values of F81AzF and Y253AzF with varying substrate duplex lengths and protein concentrations, we found that F81AzF consistently showed higher FRET efficiency. In order to observe FRET, the donor and acceptor transition dipoles must be aligned.[41–43] As such, the higher E_{PR} values observed with F81AzF may suggest that the Cy5 fluorophore at this site is attached at a more suitable position/orientation for FRET with the Cy3 fluorophore located on the DNA substrate, as compared to Y253AzF. Overall, we found that as the length of the duplex increased, the E_{PR} value decreased, indicating that Nsp13 bound on average farther from the Cy3. This was evident as the greatest E_{PR} value for both Nsp13-AzF constructs was observed with the S20-Cy3/X5 substrate as it had the shortest duplex region. For the fully duplexed substrate (S20-Cy3/X20), the resulting E_{PR} was reduced to ~0.14 with F81AzF and ~0.12 with Y235AzF. This residual E_{PR} may be due to the bleed-through of the Cy3 signal into the Cy5 channel, which is observed with the Cy3-labelled dsDNA substrate alone. For the F81AzF construct specifically, as protein concentration increases, we observed an increase in the Cy5 signal at 670 nm by FRET, along with the expected concomitant decrease in the donor Cy3 signal at 565 nm. However, with the Y253AzF construct, we observed an increase in the Cy5 signal, with increasing protein concentration, but it was not anti-correlated with the donor Cy3 signal. This may be due to the fact that previous reports have indicated that protein-induced fluorescence enhancement

(PIFE) can influence low FRET situations and cause the intensity of the dye on the protein (Cy5) to increase without the anti-correlated decrease exhibited by the other dye.[44]

It is also important to note that this assay measures the average FRET of a heterogeneous population. Therefore, variations in the FRET efficiencies observed may reflect heterogeneity in the protein population as well as the dynamics and kinetics of the Nsp13 binding to its substrate. It is also possible that these FRET measurements reflect the presence of multiple protein binding modes and not solely the desired binding of Nsp13 at the ss/ds junction on the Cy3-labelled substrate. Since previous studies have demonstrated that some helicases can have basal ATPase activities stimulated by ss nucleic acids,[45] our results may reflect the average FRET efficiency of Nsp13 as it slides along the ss-overhang of the substrates in the absence of ATP.

Collectively, these results show that we can fluorescently label Nsp13 through genetic code expansion techniques and use it to detect DNA binding by FRET. This approach in using ncAAs as a bioorthogonal handle for fluorescent labelling provides many advantages over other common methods of protein labelling, such as labelling through the cysteines or amine groups in the protein.[46] To start, this method enables the site-selective modification of a single residue, consequently minimizing alterations to the native protein structure and function. This starkly contrasts the relatively large size of many fluorescent proteins (typically $\sim$25 kDa), such as the commonly used green fluorescent protein (GFP),[47] which can compromise the function of co-expressed biomolecules. Also, by attaching the fluorophore to a single position, we can improve the chances that the generated FRET observed in ensemble assays is specific to a given binding mode or conformation. The flexibility to label any residue on a protein is also imperative for ensuring that the fluorophore is in an agreeable position and orientation for FRET. However, despite this specific labelling of Nsp13, the FRET-based binding assays we have conducted here still report on the average conformation and activity of a heterogeneous population of Nsp13 molecules, making it difficult to discern the behaviour of individual molecules in different catalytic states.

In order to delineate the molecular mechanism by which Nsp13 interacts with its nucleic acid substrate, smFRET can provide key insights into binding kinetics, conformational transitions and helicase-substrate interactions at the single-molecule level. While the temporal resolution of smFRET is insufficient to resolve single-nucleotide translocation steps given the unwinding and translocation rates of Nsp13 ($\sim$100 nt s^{-1} and $\sim$1000 nt s^{-1}, respectively), this technique remains a powerful tool for interrogating slower, functionally relevant processes. Specifically, smFRET can probe dynamic binding equilibria, detect distinct conformational states of Nsp3 during substrate engagement, and assess the influence of nucleotide state or cofactors on helicase function. Our study points to a role of leveraging site-specific fluorophore labelling to distinguish different nucleic acid-bound states of Nsp13, observing unwinding conditions in various conditions, and further quantify helicase binding and unbinding kinetics. These insights will complement existing high-resolution single-molecule techniques by providing a structural and mechanistic framework for understanding Nsp13 function during viral replication. Our method also allows for convenient screening of inhibitors of both binding and unwinding of double stranded RNA intermediates.

Conclusions

Overall, we identified two Nsp13-AzF constructs, F81AzF and Y253AzF, that can be efficiently labelled with a Cy5-DBCO dye through SPAAC reactions. We confirmed that these mutations had little effect on its helicase unwinding activity and therefore were ideal candidates for FRET-based *in vitro* characterization of Nsp13 binding activity. Ultimately, F81AzF was identified to be the best Nsp13-AzF construct for use in future smFRET experiments to study and unwinding.

Materials and methods

Nucleic acids

All subcloning and site-directed mutagenesis primers were purchased from Sigma-Aldrich (Darmstadt, Germany). All DNA oligonucleotides for the helicase unwinding assay and FRET assay were purchased from Integrated DNA Technologies (Coralville, IA, USA).

Subcloning and site-directed mutagenesis of Nsp13

The full-length coding sequence of the SARS-CoV-2 Nsp13 helicase was subcloned into the pET-21(a)+ vector for bacterial expression. Briefly, a bacterial codon-optimized sequence for SARS-CoV-2 Nsp13 helicase (Addgene, plasmid #159614) was subcloned by PCR into the pET21(a)+ bacterial expression vector using forward and reverse PCR primers (Table S1, ESI†). The PCR products were then digested with BamHI and HindIII and inserted into the multiple cloning site of pET21(a)+, keeping the C-terminal 6×-His-tag in frame. The resulting Nsp13 bacterial expression vector (pET21-Nsp13) was confirmed by sequencing performed at Genome Quebec (Montreal, QC). Site-directed mutagenesis was performed to introduce an amber stop codon (TAG) mutation into pET21-Nsp13 at the following positions: F81, F90, Y205, Y246, and Y253. Reactions were carried out in PCR tubes consisting of 20 ng of pET21-Nsp13 plasmid DNA, 1× Xtremebuffer, 0.4 mM dNTPs, 0.3 μM each of the corresponding forward and reverse site-directed mutagenesis primers (Table S1, ESI†), and 0.02 U μL^{-1} KOD polymerase (Novagen) in a total reaction volume of 50 μL in water. Reactions were placed in a thermocycler and run at 98 °C for 2 minutes, 95 °C for 30 seconds, 55 °C for 1 minute, 72 °C for 7 minutes (1 minute KB^{-1}), repeating steps 2–4 for a total of 18 cycles before a final extension at 72 °C for 5 minutes. The resulting Nsp13-AzF plasmid sequences were confirmed by sequencing performed at Genome Quebec (Montreal, QC).

Small-scale bacterial expression and screening of AzF incorporation

To assess the bacterial expression of Nsp13-AzF constructs, *E. coli* strain BL21 (DE3) (Thermofisher Scientific) cells were

transformed with Nsp13-AzF plasmids along with an orthogonal tRNA/aminoacyl tRNA synthetase pair (tRNA/aaRS) gifted from the lab of Dr Peter G. Schultz (Addgene plasmid # 31186).[48] The transformed cells were then grown in 2 mL cultures of LB media supplemented with 100 μg mL^{-1} ampicillin and 50 μL mL^{-1} spectinomycin at 37 °C to an OD of 0.5–0.6. Expression of the Nsp13-AzF constructs was induced with the addition of 1 mM isopropyl β-D-1-thiogalactopyranoside (IPTG) (Teknova) and 1 mM AzF (MedChemExpress LLC) and allowed to grow at 18 °C overnight. The cells were pelleted by centrifugation, resuspended in 2× Laemmli Buffer (Biorad), and heated at 95 °C for 15 minutes. The samples were resolved on a 10% stain-free SDS-PAGE gel (Bio-Rad) and scanned on a ChemiDoc MP imager (Bio-Rad) before the proteins were transferred to a PDVF membrane and probed for Nsp13-AzF expression using a 6×-His Tag monoclonal antibody (Thermofisher Scientific).

WT Nsp13 and Nsp13-AzF protein purification

Large-scale bacterial expression of WT and Nsp13-AzF were prepared as described under "small-scale bacterial expression and screening of AzF incorporation". Briefly, transformed *E. coli* strain BL21 (DE3) cells containing the Nsp13-AzF plasmids were grown in 600 mL of LB supplemented with 100 μg mL^{-1} ampicillin and 50 μL mL^{-1} spectinomycin at 37 °C to an OD of 0.5–0.6. Protein expression was induced with the addition of 1 mM IPTG (Teknova) and 1 mM AzF (MedChemExpress LLC) before allowing the cultures to grow at 18 °C overnight. Cells were harvested by centrifugation at 5000×*g* for 5 minutes. The pellet was resuspended in lysis buffer (50 mM Tris (pH 8.0), 300 mM NaCl, 10 mM imidazole (pH 8.0)) supplemented with cOmplete™ Protease Inhibitor Cocktail (Roche) and subsequently lysed by sonication (50% amplitude) for 2 minutes cycling between 1 second off and 1 second on ice. The cells were then centrifuged at 20 000×*g* for 20 minutes at 4 °C to obtain the soluble fraction. WT Nsp13 and Nsp13-AzF constructs were purified using HisTrap HP columns (Sigma) and washed with wash buffer (500 mM Tris (pH 8.0), 600 mM NaCl, 60 mM imidazole (pH 8.0)). Purified protein was eluted using elution buffer (50 mM Tris (pH 8.0), 300 mM NaCl, 300 mM imidazole (pH 8.0)) and concentrated using 30 kDa MWCO ultra-centrifugation tubes (Amicon) before buffer-exchanged into a buffer containing 50 mM Tris (pH 8.0), and 100 mM NaCl. Size-exclusion fast protein liquid chromatography (FPLC) was then performed using a S75 column (GE Healthcare Life Sciences). Purified protein concentrations were determined on a NanoDrop 2000 (Thermo Scientific) using the calculated extinction coefficient of 68 785 M^{-1} cm^{-1}.[8]

Fluorescent labelling of Nsp13-AzF with Cy5-DBCO

5 μM of purified WT Nsp13 and Nsp13-AzF constructs were allowed to react with 10 μM Cy5-DBCO (Sigma Aldrich) in 1× PBS (pH 7.4) at room temperature for 30 minutes. To remove excess dye, the labelled proteins were run through a P30 gel microspin column (Bio-Rad) according to the manufacturer's protocol. SDS-PAGE loading buffer was added to the samples and heated at 95 °C for 10 minutes before being resolved on a 10% stain-free SDS-PAGE gel (Bio-Rad). The gel was scanned for Cy5 fluorescence and stain-free protein visualization on a ChemiDoc MP imager (Bio-Rad). The labelled proteins were then transferred to a PDVF membrane and probed for Nsp13-AzF expression using a 6×-His Tag monoclonal antibody (Thermofisher Scientific).

Helicase unwinding assay

The helicase unwinding assay was adapted from a previous publication with some modifications.[35] Briefly, the Cy3-DNA strand and black hole quencher-2 (BHQ-2) (Table S2, ESI†) were annealed at a 1 : 1.1 ratio with concentrations of 20 μM : 22 μM, respectively, in a thermocycler by heating to 75 °C for 5 minutes followed by a gradual cooling to 4 °C over 50 minutes. In a 96-well black bottom plate, a 2× enzyme solution containing 5 nM of purified WT Nsp13 or Nsp13-AzF in reaction buffer (20 mM HEPES (pH 7.6), 20 mM NaCl, 5 mM $MgCl_2$, and 0.1 mg mL^{-1} BSA) was added in triplicate. To start the reaction, a 2× solution containing 50 nM duplex substrate, 250 nM competitor strand DNA, and 100 μM ATP in reaction buffer was added to the enzyme solution in the plate. Samples were excited at 530 nm (9 nm slit width) and emission was recorded at 570 nm (15 nm slit width) using a SpectraMax i3 plate reader (molecular devices) every minute for 60 minutes. Fluorescence values were fitted using a one-phase association on PRISM-GraphPad (v9.4.1) to determine unwinding rates.

Fluorescent resonance energy transfer assay

A 20 nt long DNA strand was ordered with a Cy3 dye attached to the 3′ terminus (S20-Cy3). A series of complementary DNA sequences were designed to form partial duplexes of varying lengths with the S20-Cy3 strand. These sequences are denoted as "X*n*", where "*n*" refers to the length of the duplex region (Table S3, ESI†). For the FRET assay, the substrates were prepared by annealing the S20-Cy3 strand with the X*n* strands at a 1 : 2 ratio with concentrations of 20 μM : 40 μM, respectively, by heating to 75 °C for 5 minutes followed by gradual cooling to 4 °C over 50 minutes in a thermocycler. The FRET assay was performed in a total volume of 40 μL in 96-well black bottom plates. Purified and Cy5-DBCO labelled WT Nsp13, F81AzF and Y253AzF Nsp13 constructs (50–400 nM) were serially diluted in FRET reaction buffer (25 mM MOPS (pH 6.0), 10 mM NaCl, 3 mM $MgCl_2$, and 0.1% Tween-20) and incubated with 100 nM of corresponding Cy3-DNA substrate (S20-Cy3/X20, S20-Cy3/X17, S20-Cy3/X15, S20-Cy3/X12, S20-Cy3/X10, S20-Cy3/X8, S20-Cy3/X5) for 30 minutes at room temperature. Samples were excited at 520 nm and the fluorescence spectra were recorded from 555 to 700 nm using a SpectraMax i3 plate reader (molecular devices). The ratiometric intensity-based FRET proximity ratio (E_{PR}) was defined as $I_A/(I_A + I_D)$, where I_A and I_D are the emission maximum intensities of the Cy5 acceptor at 670 nm and the Cy3 donor at 565 nm, respectively.[49]

Author contributions

C. Hum performed experimental work, data collection, analysis and writing the original draft. N. Ahmed contributed to conceptualization of the study. E. Lundrigan performed experimental work, data collection, and analysis and contributed to the writing and revising at the stage of review. J. P. Pezacki

conceptualized and supervised the work as well as verified analyses and data collection techniques and contributed to writing and revising of the manuscript.

Data availability

On behalf of the authors, I state that all data associated with this manuscript will be made available to the general public. We are committed to transparency and scientific integrity.

Conflicts of interest

There are no conflicts to declare.

Acknowledgements

We thank the Natural Sciences and Engineering Council of Canada (NSERC) for a discovery grant to JPP, and the Canadian Institutes for Health Research for project grants to JPP. We thank NSERC for funding in the form of a graduate scholarship to NA.

References

1 F. Wu, S. Zhao and B. Yu, *et al.*, A new coronavirus associated with human respiratory disease in China, *Nature*, 2020, **579**(7798), 265–269, DOI: 10.1038/s41586-020-2008-3.
2 A. Pak, O. A. Adegboye, A. I. Adekunle, K. M. Rahman, E. S. McBryde and D. P. Eisen, Economic Consequences of the COVID-19 Outbreak: the Need for Epidemic Preparedness, *Front. Public Health*, 2020, **8**, 241, DOI: 10.3389/fpubh.2020.00241.
3 D. Tang, P. Comish and R. Kang, The hallmarks of COVID-19 disease, *PLoS Pathog.*, 2020, **16**(5), e1008536, DOI: 10.1371/journal.ppat.1008536.
4 E. Dong, H. Du and L. Gardner *An interactive web-based dashboard to track COVID-19 in real time*. Published online 2020, DOI: 10.1016/S1473-3099(20)30120-1.
5 E. Mathieu, H. Ritchie, L. Rodés-Guirao, *et al. Coronavirus Pandemic (COVID-19)*. *Our World in Data*. Published online March 5, 2020. Accessed January 15, 2023. https://ourworldindata.org/coronavirus.
6 R. Zhang, Y. Li and T. J. Cowley, *et al.*, The nsp1, nsp13, and M Proteins Contribute to the Hepatotropism of Murine Coronavirus JHM.WU, *J. Virol.*, 2015, **89**(7), 3598–3609, DOI: 10.1128/jvi.03535-14.
7 K. C. Lehmann, E. J. Snijder, C. C. Posthuma and A. E. Gorbalenya, What we know but do not understand about nidovirus helicases, *Virus Res.*, 2015, **202**, 12–32, DOI: 10.1016/j.virusres.2014.12.001.
8 A. B. Gurung, In silico structure modelling of SARS-CoV-2 Nsp13 helicase and Nsp14 and repurposing of FDA approved antiviral drugs as dual inhibitors, *Gene Rep.*, 2020, **21**, 100860, DOI: 10.1016/j.genrep.2020.100860.
9 K. J. Jang, S. Jeong, D. Y. Kang, N. Sp, Y. M. Yang and D. E. Kim, A high ATP concentration enhances the cooperative translocation of the SARS coronavirus helicase nsP13 in the unwinding of duplex RNA, *Sci. Rep.*, 2020, **10**, 4481, DOI: 10.1038/s41598-020-61432-1.
10 J. A. Newman, A. Douangamath and S. Yadzani, *et al.*, Structure, mechanism and crystallographic fragment screening of the SARS-CoV-2 NSP13 helicase, *Nat. Commun.*, 2021, **12**(1), 1–11, DOI: 10.1038/s41467-021-25166-6.
11 K. J. Mickolajczyk, P. M. M. Shelton and M. Grasso, *et al.*, Force-dependent stimulation of RNA unwinding by SARS-CoV-2 nsp13 helicase, *Biophys. J.*, 2021, **120**(6), 1020–1030, DOI: 10.1016/j.bpj.2020.11.2276.
12 J. A. Tanner, R. M. Watt and Y. B. Chai, *et al.*, The severe acute respiratory syndrome (SARS) coronavirus NTPasefhelicase belongs to a distinct class of 5′ to 3′ viral helicases, *J. Biol. Chem.*, 2003, **278**(41), 39578–39582, DOI: 10.1074/jbc.c300328200.
13 K. A. Ivanov, V. Thiel, J. C. Dobbe, Y. van der Meer, E. J. Snijder and J. Ziebuhr, Multiple Enzymatic Activities Associated with Severe Acute Respiratory Syndrome Coronavirus Helicase, *J. Virol.*, 2004, **78**(11), 5619–5632, DOI: 10.1128/jvi.78.11.5619-5632.2004.
14 A. O. Adedeji, B. Marchand and A. J. W. te Velthuis, *et al.*, Mechanism of Nucleic Acid Unwinding by SARS-CoV Helicase, *PLoS One*, 2012, **7**(5), e36521, DOI: 10.1371/journal.pone.0036521.
15 M. Wilamowski, D. A. Sherrell and G. Minasov, *et al.*, 2′-O methylation of RNA cap in SARS-CoV-2 captured by serial crystallography, *Proc. Natl. Acad. Sci. U. S. A.*, 2021, **118**(21), e2100170118, DOI: 10.1073/pnas.2100170118.
16 M. Rosas-Lemus, G. Minasov and L. Shuvalova, *et al.*, High-resolution structures of the SARS-CoV-2 2′-O-methyltransferase reveal strategies for structure-based inhibitor design, *Sci. Signaling*, 2020, **13**(651), 1202, DOI: 10.1126/scisignal.abe1202.
17 G. J. Park, A. Osinski and G. Hernandez, *et al.*, The mechanism of RNA capping by SARS-CoV-2, *Nature*, 2022, **609**(7928), 793–800, DOI: 10.1038/s41586-022-05185-z.
18 T. Viswanathan, S. Arya and S. H. Chan, *et al.*, Structural basis of RNA cap modification by SARS-CoV-2, *Nat. Commun.*, 2020, **11**(1), 1–7, DOI: 10.1038/s41467-020-17496-8.
19 W. Yan, Y. Zheng, X. Zeng, B. He and W. Cheng, Structural biology of SARS-CoV-2: open the door for novel therapies, *Signal Transduction Targeted Ther.*, 2022, **7**(1), 1–28, DOI: 10.1038/s41392-022-00884-5.
20 J. Chen, B. Malone and E. Llewellyn, *et al.*, Structural Basis for Helicase-Polymerase Coupling in the SARS-CoV-2 Replication-Transcription Complex, *Cell*, 2020, **182**(6), 1560–1573.e13, DOI: 10.1016/J.CELL.2020.07.033.
21 R. Martin, J. Li and A. Parvangada, *et al.*, Genetic conservation of SARS-CoV-2 RNA replication complex in globally circulating isolates and recently emerged variants from humans and minks suggests minimal pre-existing resistance to remdesivir, *Antiviral Res.*, 2021, **188**, 105033, DOI: 10.1016/j.antiviral.2021.105033.
22 A. O. Adedeji, K. Singh and N. E. Calcaterra, *et al.*, Severe Acute Respiratory Syndrome Coronavirus Replication Inhibitor That Interferes with the Nucleic Acid Unwinding of the Viral Helicase, *Antimicrob. Agents Chemother.*, 2012, **56**(9), 4718–4728, DOI: 10.1128/AAC.00957-12.

23 M. S. Yu, J. Lee and J. M. Lee, *et al.*, Identification of myricetin and scutellarein as novel chemical inhibitors of the SARS coronavirus helicase, nsP13, *Bioorg. Med. Chem. Lett.*, 2012, **22**(12), 4049–4054, DOI: **10.1016/J.BMCL.2012.04.081**.

24 L. Yan, Y. Zhang and J. Ge, *et al.*, Architecture of a SARS-CoV-2 mini replication and transcription complex, *Nat. Commun.*, 2020, **11**(1), 1–6, DOI: **10.1038/s41467-020-19770-1**.

25 Z. Jia, L. Yan and Z. Ren, *et al.*, Delicate structural coordination of the Severe Acute Respiratory Syndrome coronavirus Nsp13 upon ATP hydrolysis, *Nucleic Acids Res.*, 2019, **47**(12), 6538–6550, DOI: **10.1093/nar/gkz409**.

26 A. Zander, P. Holzmeister, D. Klose, P. Tinnefeld and D. Grohmann, Single-molecule FRET supports the two-state model of Argonaute action, *RNA Biol.*, 2014, **11**(1), 45, DOI: **10.4161/RNA.27446**.

27 S. K. Marx, K. J. Mickolajczyk, J. M. Craig, C. A. Thomas, A. M. Pfeffer, S. J. Abell, J. D. Carrasco, M. C. Franzi, J. R. Huang, H. C. Kim, H. Brinkerhoff, T. M. Kapoor, J. H. Gundlach and A. H. Laszlo, Observing inhibition of the SARS-CoV-2 helicase at single-nucleotide resolution, *Nucleic Acids Res.*, 2023, **17**, 9266–9278, DOI: **10.1093/nar/gkad660**.

28 L. Jakob, A. Gust and D. Grohmann, Evaluation and optimisation of unnatural amino acid incorporation and bioorthogonal bioconjugation for site-specific fluorescent labelling of proteins expressed in mammalian cells, *Biochem. Biophys. Rep.*, 2019, **17**, 1, DOI: **10.1016/j.bbrep.2018.10.011**.

29 C. J. Ablenas, Y. Gidi and M. H. Powdrill, *et al.*, Hepatitis C Virus Helicase Binding Activity Monitored through Site-Specific Labeling Using an Expanded Genetic Code, *ACS Infect. Dis.*, 2019, **5**(12), 2118–2126, DOI: **10.1021/acsinfecdis.9b00220**.

30 J. W. Chin, S. W. Santoro, A. B. Martin, D. S. King, L. Wang and P. G. Schultz, Addition of *p*-azido-L-phenylalanine to the genetic code of *Escherichia coli*, *J. Am. Chem. Soc.*, 2002, **124**(31), 9026–9027, DOI: **10.1021/ja027007w**.

31 K. Lang and J. W. Chin, Cellular incorporation of unnatural amino acids and bioorthogonal Labeling of Proteins, *Chem. Rev.*, 2014, **114**(9), 4764–4806, DOI: **10.1021/cr400355w**.

32 G. R. Perez-Lemus, C. A. Menéndez, W. Alvarado, F. Byléhn and J. J. De Pablo, Toward wide-spectrum antivirals against coronaviruses: Molecular characterization of SARS-CoV-2 NSP13 helicase inhibitors, *Sci. Adv.*, 2022, **8**(1), 4526, DOI: **10.1126/sciadv.abj4526**.

33 J. Zeng, F. Weissmann and A. P. Bertolin, *et al.*, Identifying SARS-CoV-2 antiviral compounds by screening for small molecule inhibitors of nsp13 helicase, *Biochem. J.*, 2021, **478**(13), 2405–2423, DOI: **10.1042/bcj20210201**.

34 S. B. Sun, P. G. Schultz and C. H. Kim, Therapeutic applications of an expanded genetic code, *ChemBioChem*, 2014, **15**(12), 1721, DOI: **10.1002/cbic.201402154**.

35 K. Wang, A. Sachdeva and D. J. Cox, *et al.*, Optimized orthogonal translation of unnatural amino acids enables spontaneous protein double-labelling and FRET, *Nat. Chem.*, 2014, **6**(5), 393–403, DOI: **10.1038/nchem.1919**.

36 A. Herbert and M. Poptsova, Z-RNA and the Flipside of the SARS Nsp13 Helicase: Is There a Role for Flipons in Coronavirus-Induced Pathology?, *Front. Immunol.*, 2022, **13**, 2814, DOI: **10.3389/fimmu.2022.912717**.

37 J. W. Chin, Expanding and Reprogramming the Genetic Code of Cells and Animals, *Annu. Rev. Biochem.*, 2014, **83**, 379–408, DOI: **10.1146/annurev-biochem-060713-035737**.

38 C. S. McKay and M. G. Finn, Click Chemistry in Complex Mixtures: Bioorthogonal Bioconjugation, *Chem. Biol.*, 2014, **21**(9), 1075–1101, DOI: **10.1016/j.chembiol.2014.09.002**.

39 R. Hoogenboom, Thiol–Yne Chemistry: A Powerful Tool for Creating Highly Functional Materials, *Angew. Chem., Int. Ed.*, 2010, **49**(20), 3415–3417, DOI: **10.1002/anie.201000401**.

40 D. Berta, M. Badaoui and S. A. Martino, *et al.*, Modelling the active SARS-CoV-2 helicase complex as a basis for structure-based inhibitor design, *Chem. Sci.*, 2021, **12**(40), 13492–13505, DOI: **10.1039/D1SC02775A**.

41 T. Ha, Single-molecule fluorescence methods for the study of nucleic acids, *Curr. Opin. Struct. Biol.*, 2001, **11**(3), 287–292, DOI: **10.1016/s0959-440x(00)00204-9**.

42 A. Iqbal, L. Wang, K. C. Thompson, D. M. J. Lilley and D. G. Norman, The structure of cyanine 5 terminally attached to double-stranded DNA: Implications for FRET studies, *Biochemistry*, 2008, **47**(30), 7857–7862, DOI: **10.1021/bi800773f**.

43 D. Shrestha, A. Jenei, P. Nagy, G. Vereb and J. Szöllősi, Understanding FRET as a research tool for cellular studies, *Int. J. Mol. Sci.*, 2015, **16**(4), 6718–6756, DOI: **10.3390/ijms16046718**.

44 H. Hwang and S. Myong, Protein induced fluorescence enhancement (PIFE) for probing protein–nucleic acid interactions, *Chem. Soc. Rev.*, 2014, **43**(4), 1221–1229, DOI: **10.1039/c3cs60201j**.

45 A. Seybert, A. Hegyi, S. G. Siddell and J. Ziebuhr, The human coronavirus 229E superfamily 1 helicase has RNA and DNA duplex-unwinding activities with 5′-to-3′ polarity, *RNA*, 2000, **6**(7), 1056–1068, DOI: **10.1017/s1355838200000728**.

46 C. P. Toseland, Fluorescent labeling and modification of proteins, *J. Chem. Biol.*, 2013, **6**(3), 85, DOI: **10.1007/s12154-013-0094-5**.

47 D. M. Chudakov, S. Lukyanov and K. A. Lukyanov, Fluorescent proteins as a toolkit for in vivo imaging, *Trends Biotechnol.*, 2005, **23**(12), 605–613, DOI: **10.1016/j.tibtech.2005.10.005**.

48 J. W. Chin, S. W. Santoro, A. B. Martin, D. S. King, L. Wang and P. G. Schultz, Addition of p-azido-L-phenylalanine to the genetic code of Escherichia coli, *J. Am. Chem. Soc.*, 2002, **124**(31), 9026–9027, DOI: **10.1021/ja027007w**.

49 R. Roy, S. Hohng and T. Ha, A practical guide to single-molecule FRET, *Nat. Methods*, 2008, **5**(6), 507–516, DOI: **10.1038/nmeth.1208**.